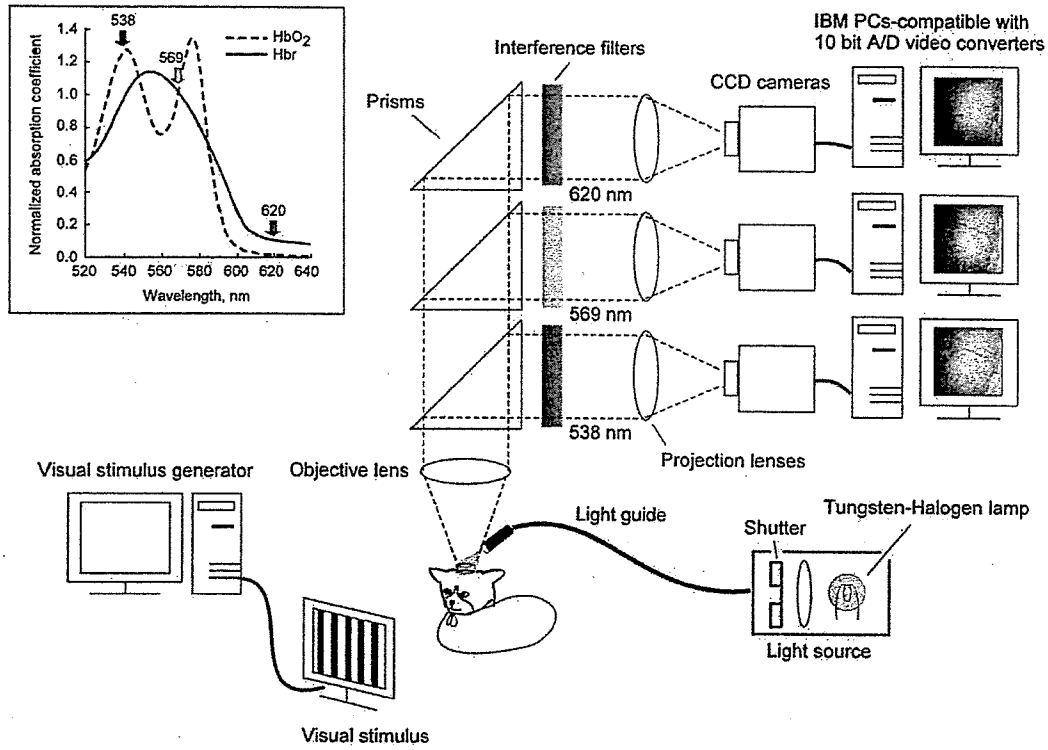

Figure 1. Scheme of the multiple wavelength imaging system. The cortical surface is illuminated with white light. Reflected light is collected by an objective lens and divided into three light paths by prisms. Each beam passes through an interference filter and is focused onto the target plane of the video cameras by projection lenses. The inset on the upper left corner shows absorption spectra of HbO_2 and Hbr. The arrows indicate central wavelengths of the three filters we used (538, 569 and 620 nm). The absorption coefficients of HbO_2 and Hbr at different wavelengths were obtained from *in vitro* experiments and normalized to the absorption coefficient at 569 nm. The normalized coefficients of HbO_2 and Hbr at 538 nm were 1.23 and 0.91 respectively. Similarly, at 620 nm the normalized coefficients of HbO_2 and Hbr were 0.01 and 0.11 respectively.

Physiological Society of Japan), and with the approval of the RIKEN Committee on Animal Research.

Animal Preparations

Cats were initially anesthetized with an inhalation of isoflurane (2-2.5%) in a mixture of 50% N_2O and 50% O_2. After tracheal cannulation, anesthesia was maintained with a mixture of 70% N_2O and 30% O_2 supplemented with 1-2% isoflurane. The cephalic vein was catheterized and neuromuscular blockade was carried out by continuous infusion of pancuronium bromide (0.2 mg/kg/h) mixed with dexamethazone (0.05 mg/kg/h) and 7.5% glucose in lactose-containing Ringer's solution. The cats were then artificially ventilated. To prevent the cornea from drying, contact lenses were fitted to the eyes. We continuously monitored rectal temperature, electroencephalogram (EEG), electrocardiogram (ECG), and expired CO_2 to assess the depth of anesthesia. Rectal temperature was maintained at 37.5-38.5 °C with a feedback-regulated heating pad system. The expired CO_2 was maintained between 3.0 and 4.0%.

On the first day of recording, a cat was placed in a stereotaxic apparatus (SN-3N, Narishige). Under aseptic surgery, we first attached with dental acrylic cement a metal post to fix its head and a stainless steel chamber (18 mm inner diameter, Nakazawa-Seisaku, Japan) for optical imaging to the skull. The metal post was placed approximately above the bregma. The chamber was placed such that it included area 17 or the border between areas 17 and 18 (in Horsley-Clarke coordinates, approximately A5-P10 for area 17 and A10-P5 for the border between areas 17 and 18). We then performed craniotomy inside the chamber, and resected the dura mater. The inside of the chamber was then filled with 1.5-2.0% agarose (Agarose-HGS, gel strength 1.5%; Nacalai Tesque, Japan) containing dexamethazone (0.1 mg) and an antibiotic (gentamicin, 0.25 mg). Finally, the chamber was covered with a round glass coverslip and sealed with a screw-top lid including a silicone gasket. We could observe the cortical surface clearly through the glass coverslip and could visualize the same functional structures repeatedly for 2-3 weeks without cleaning the inside of the chamber. After the surgery and the recordings, an appropriate antibiotic (cefodizime sodium, 60 mg/kg i.m.) was administered to the cat before returning the animal to its home cage.

During recordings on the first and subsequent days, the cat's head was immobilized with a head post instead of ear bars. Pupils were dilated by applying 0.5% tropicamide and 0.5% phenylephrine hydrochloride. The isoflurane concentration was maintained at 0.5-1.0% during the recordings. The other conditions were the same as those in the initial surgery described above.

Visual Stimuli

Square wave gratings (white: 8 cd/m^2; black: 0 cd/m^2) were generated with a VSG2/3 graphics video board (Cambridge Research Systems, Rochester, UK), controlled by homemade software, and were presented on a monitor screen (640 × 480 pixels and 100 Hz refresh rate, GDM-20SE3T, Sony). The spatial frequency and the drifting velocity of the gratings were 0.5 cycles/deg and 4 deg/s for area 17, and 0.15 cycles/deg and 15 deg/s for area 18 (Bonhoeffer *et al.*, 1995). The drifting direction was reversed every 0.5 s during a 2 s stimulus presentation. Two or four stimuli [orientations, 0° (horizontal), 45°, 90° and 135°] together with a blank screen (homogenous gray, 4 cd/m^2) as a control were presented in a pseudorandom order. In the experiment using awake cats, we used stationary grating patterns flickering at 5 Hz (8 Hz in one cat) to minimize the effect of eye movements following the grating motion. The same flickering gratings were also used in the examination of the same cats under anesthesia for comparison.

The center of a cat's visual field was estimated by projecting images of optic disks and patterns of surrounding vessels onto the monitor screen in front of the cat. The screen was placed at a distance ranging from 20 to 40 cm, where the best focus of the optic disks and the patterns of surrounding vessels were obtained for each cat. At these distances the size of the screen corresponded to 43°-86° (width) × 36°-71° (height)

of the cat's visual field. In the experiment with awake cats, the screen was placed 20 cm in front of the animals.

Optical Imaging of Intrinsic Signals

We developed a multiple wavelength imaging system equipped with three identical cameras (Sanso-Seisaku, Japan) that enabled us to simultaneously record intrinsic signals at three different wavelengths (Fig. 1). We used two sets with the same configuration: one was equipped with CID-2221D video cameras (CIDTEC, Liverpool, NY), and the other was equipped with CS8310 video cameras (Tokyo Electric Industry, Japan). The exposed cortical surface was illuminated with white light using eight fiber optic bundles placed around the chamber, which were connected to two tungsten-halogen bulbs (82 V, 300 W; Philips) driven by stabilized DC power supplies (PD110-5D; Kenwood, Japan). The duration of exposure of the cortical surface to the light was restricted to 10 s using a mechanical shutter, which opened 2 s before starting image acquisition. Reflected light from the cortical surface was collected by an objective lens, and divided into three separate paths by prisms. Each light beam passed through an interference filter tuned to one of three different wavelengths (538, 569 and 620 ± 10 nm; Asahi Spectra, Japan) and focused onto one of three video cameras by each projection lens. A combination of objective and projection lenses constituted the tandem-lens optics (Ratzlaff and Grinvald, 1991). Using different combinations of a projection lens (50 mm, f1.2; Nikon, Japan) and an objective lens (35 mm, f1.4 or 50 mm, f1.2; Nikon, Japan), imaging areas were 4.9 × 4.9 mm^2 or 7.0 × 7.0 mm^2 for the CID-2221D camera (256 × 256 pixels) and 8.8 × 6.6 mm^2 for the CS8310 camera (640 × 480 pixels). The imaging areas of the three cameras were adjusted to overlap in order to record signals from the same region of the cortical surface. Video signals from the three cameras were separately digitized with 10-bit video A/D converter boards (Pulsar, Matrox Graphics Inc., Canada) on three computers. These computers synchronously acquired 240 frames at a frame rate of 1/30 s for the CS8310 camera or 1/60 s for the CID-2221D camera. Fifteen consecutive frames for the CS8310 camera or 15 alternate frames for the CID-2221D camera were averaged on-line. Consequently, 16 images were acquired with a temporal resolution of 500 ms (i.e. 8 s). Acquired images were stored on hard disks without binning for the CID-2221D camera (256 × 256 pixels) and with binning (2 × 2 pixels were combined into a single pixel) for the CS8310 camera (i.e. 320 × 240 pixels).

Images of the cortical surface were taken using these cameras and the focal plane was changed from the cortical surface to 700–800 μm below. The maximum intensities of video signals from the three cameras were adjusted to near-saturation level by changing the intensity of incident light and camera gains. The black levels of each video signal (a video signal obtained under complete darkness, ~10% of saturation level) were then recorded for off-line data processing. In the experiment with anesthetized cats, data acquisition was started at a certain phase of respiration in synchrony with heartbeat. A visual stimulus appeared 1 s after the onset of image acquisition. To allow the relaxation of vascular responses to the previous stimulation, the interstimulus interval (ISI) was set at 30 s. Data of four trials using the same stimulus were averaged online and saved as one block. We recorded 20 blocks in one experiment; altogether, responses for 80 trials (20 blocks, 4 trials per block) were acquired for each stimulus.

In the recordings with awake cats, the body of the cat was placed into a loosely fitting pouch and the head was immobilized by the implanted head post. The cats quickly became accustomed to the restriction of movements and presented no signs of discomfort during the experiments. To minimize visual input from surroundings, the experiments were performed in a dark room and mechanical shutters were placed in front of the cat's eyes. The shutters were only opened during the stimulus presentation. Unlike the experiment under anesthesia, data acquisition was not synchronized with respiration and heartbeat. The total recording period was restricted to 1.5 h/day to maintain the cats' alertness level. Data from 40 trials were averaged (20 blocks, 2 trials per a block) for each stimulus in one day. The experiments were repeated for two successive days and the data from the two days were finally averaged. The temporal and spatial patterns of intrinsic signals on the first day were almost identical to those on the second day (data not shown). The data from the same cat under anesthesia were also collected. To ensure that recordings were taken from the same region, we did not change the camera position relative to the head post until a series of experiments for the cat had been completed. We did not observe a misalignment of cortical vascular patterns in the series of experiments.

Imaging of Changes in Blood Volume with Intravascular Absorption Dye

For the measurement of changes in blood volume, we injected a light-absorbing dye (Nigrosin, water-soluble Acid Black 2; Sigma) through the cat's cephalic vein and recorded the stimulus-evoked absorption changes at 620 nm. We chose absorption dye instead of fluorescent dyes, which have previously been used for the measurement of blood volume (Frostig *et al.*, 1990; Narayan *et al.*, 1995; Cannestra *et al.*, 1998), because (i) fluorescent dye signals are in general too weak to resolve small changes such as stimulus-specific components, (ii) there is minimal effect of dye bleaching, and (iii) the same optics can be employed to assess the dye-specific responses immediately after the intrinsic signal imaging. The dye was dissolved in saline, filtered using a Millipore filter (0.22 μm pore size, Millipore Co. Bedford, MA), and injected prior to recording (final dosage, 20–34 mg/kg nigrosin for five cats). The physiological conditions (e.g. heart rate) of the cats did not change following the injection of the dye. Since the dye absorbed the incident light, the reflected light intensity from the cortical surface decreased after the dye injection. The intensity of the reflected light was readjusted to the saturation level of video signals prior to recording by increasing the incident light intensity. Data from 20–80 trials were averaged (5 to 20 blocks, 4 trials per block) for each stimulus.

Data Analysis

We analyzed all images pixel by pixel using IDL 5.4 (Research Systems, Inc.). The statistical significance of the data was evaluated by *t*-test (two-tailed, paired). The first step in the data analysis was to extract reflected light intensity from video signals by subtracting the image obtained in complete darkness (the black level) from the 16 consecutive images (8 s at 0.5 s/image). A change in reflected light intensity (intrinsic signals) was then expressed as the change in the optical density (ΔOD) as follows:

$$\Delta OD(t)_\lambda = \ln\{I_\lambda^{pre}/I_\lambda(t)\} \quad (1)$$

where I_λ^{pre} is the average of reflected light intensity before stimulus onset (1 s) at a wavelength λ, and $I_\lambda(t)$ is the reflected light intensity at t s from the stimulus onset. We calculated ΔODs for the individual stimuli and for the control (blank screen), and then subtracted ΔOD for the control from ΔOD for the grating stimuli to remove artifacts due to the respiratory cycle.

To demonstrate the spatial patterns of iso-orientation domains, differential images were generated by subtracting responses to one orientation from those to the orthogonal orientation. The differential images were then temporally averaged from 1 to 7 s after stimulus onset and processed using a Gaussian spatial filter (cutoff frequencies, σ = 10/mm for a high cutoff frequency and 1/mm for a low cutoff frequency for images obtained by the CS8310 camera, and σ = 5/mm for high cut-off and 1/mm for low cutoff for images obtained by the CID-2221D camera). The similarity between two differential images obtained at different wavelengths was quantified by calculating a correlation coefficient on pixel-by-pixel basis. In particular, when two pairs of orthogonal stimuli (the combination of 0° and 90° or that of 45° and 135°) were used at these wavelengths, a correlation coefficient of differential images was calculated for each pair separately, and then an average of the correlation coefficients was used to evaluate the similarity of differential images obtained at these wavelengths.

To quantitatively examine the intensities of intrinsic signals we averaged pixels in the region of interest (ROI). Pixels covering surface vessels thicker than 50 μm and those located outside of the cortex were excluded from the ROI. We divided ROI into active and less-active domains and averaged pixels of the active domains separately from pixels of the less-active domains. The active and less-active domains were determined on the basis of a differential image at 620 nm processed with the spatial filter. Pixels having positive values in the

differential image were assigned to the active domains and the remaining pixels were assigned to the less-active domains. The difference in the signal intensity between two domains was calculated by subtracting the average pixel value for the less-active domains from that for the active domains.

To quantify the spatial resolution of intrinsic signals, we measured the distance between neighboring iso-orientation domains in differential images. The distance between neighboring iso-orientation domains in the differential image was evaluated using an auto-correlation map of the differential image using NIH Image software (Scion Corporation) since the pattern of iso-orientation domains seems to have a periodic structure. The differential image used for this analysis was not processed by any spatial filter. The autocorrelation map was calculated for an ROI of 128 × 128 pixels (2.5 × 2.5 mm^2 for the CID-2221D camera with a 35 mm objective lens and 3.5 × 3.5 mm^2 for the CID-2221D and CS8310 cameras with a 50 mm objective lens) in the differential images. We then extracted the profile of the autocorrelation map along the central and secondary largest peaks. We assigned the distance between these two peaks as the distance between neighboring iso-orientation domains assuming that the periodic structure of the iso-orientation domains is the most dominant one in the map. The size of iso-orientation domains was estimated by measuring full width at half-maximum (FWHM) of the center peak of the profile.

Results

Definition of Stimulus-specific and Stimulus-nonspecific Components of Intrinsic Signals

Figure 2*A,B* shows the spatiotemporal patterns of the intrinsic signal at 620 nm in cat visual cortex induced by full-field grating stimuli. The grating stimuli evoked initial increases in light absorption (darkening of the cortex), which were followed by absorption decreases across the baseline (lightening of the cortex). These absorption changes were not spatially confined to domains specific for particular stimulus orientations. As reported previously (Grinvald *et al.*, 1986), two orthogonal orientations elicited a common absorption increase over the entire range (stimulus-nonspecific component), which was locally modulated in a stimulus-specific manner (stimulus-specific component) (Fig. 2*D*). Since this stimulus-specific modulation is complementary in two orthogonal orientations (Fig. 2*D*, red and blue lines), the region showing this stimulus specificity was extracted by subtracting the response for one orientation from that for the orthogonal orientation (Fig. 2*C*, and Fig. 2*D*, green line). We define regions where a stimulus elicited a larger absorption than the orthogonal stimulus, such as the shaded regions shown in Figure 2*D*, as 'active domains' for the stimulus. On the other hand, we define regions where the stimulus elicited smaller increases in absorption than the orthogonal stimulus as 'less-active domains' for the stimulus. For the analysis of the stimulus-nonspecific component, we averaged the intrinsic signals regardless of whether the domain was active or less active. For the analysis of the stimulus-specific component, we subtracted the intrinsic signal for the less-active domains from the signal for the active domains (see also Materials and Methods).

Time Courses of Stimulus-nonspecific and Stimulus-specific Components of Intrinsic Signals

As an approximation, we assume that Hbr and HbO_2 concentration changes are the major sources of intrinsic signals at visible wavelengths. Intrinsic signals at 620 and 569 nm then correspond approximately to changes in Hbr concentration and that of total hemoglobin (Hbt) concentration (the sum of Hbr and HbO_2 concentrations), respectively. This is because at 620 nm, the absorption coefficient of Hbr is about 10 times larger than that of HbO_2 and 569 nm corresponds to the isosbestic point of Hbr and HbO_2 absorption (Fig. 1 inset). In addition, we recorded intrinsic signals at 538 nm, where HbO_2 has a higher absorption coefficient than Hbr. Figure 3*A* shows

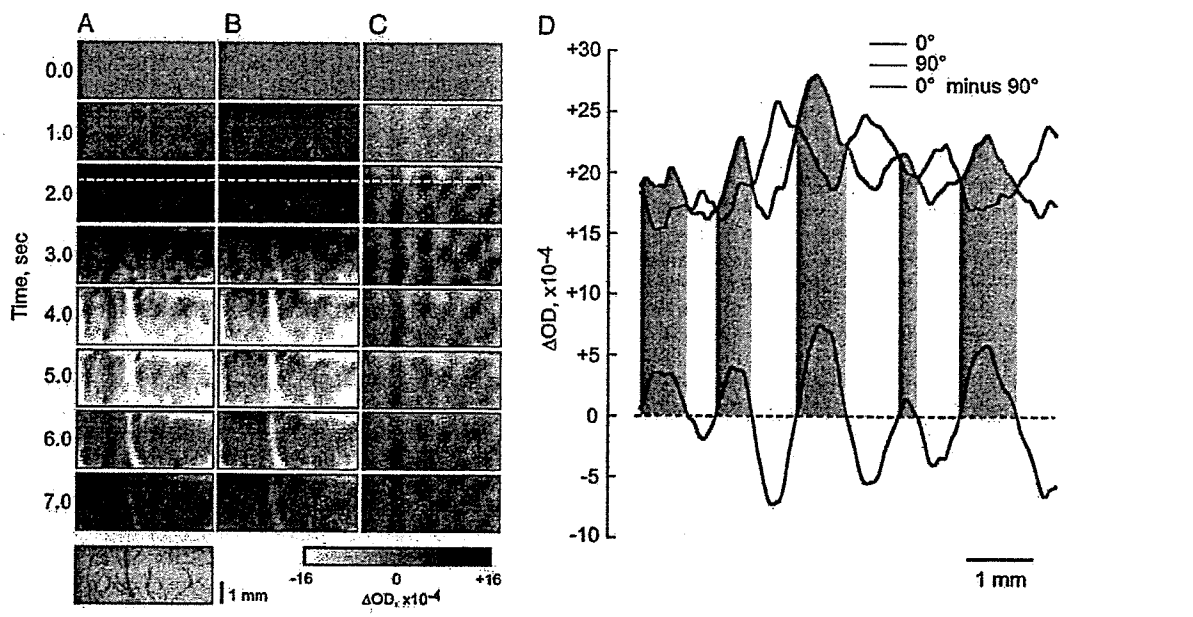

Figure 2. Stimulus-specific and stimulus-nonspecific components of intrinsic signals. (*A, B*) Images of intrinsic signal at 620 nm induced by gratings with 0° (*A*) and 90° (*B*) orientations along with the ROI at the bottom (cortical surface image taken at 538 nm). Grayscale range is shown at the bottom. The images are shown as a function of time from the stimulus onset. The stimulus duration was 2 s. (*C*) Differential images obtained by subtracting images in *B* from images in *A*. Black and white patches were specific to gratings of 0° and 90° orientations respectively. (*D*) Magnitudes of signal intensities along white broken lines on the images (*A–C*) at 2.0 s after stimulus onset. The horizontal broken line indicates the baseline corresponding to the absence of absorption change. Shaded regions indicate the portions showing larger responses to a grating at 0° orientation. The high-frequency noise of the lines was removed using the high-cut filter (cutoff frequency σ = 10/mm).

the time courses of stimulus-nonspecific components of the intrinsic signals obtained at these wavelengths. At 620 nm, we consistently observed biphasic time courses, in which the light absorption increased after stimulus onset, reached a maximum after 2 s and decreased, going below the baseline (time to reach the minimum, 5 s). On the other hand, the time courses of the signals at 538 and 569 nm were monophasic: the light absorption increased and returned to the baseline without crossing it (time to reach the maximum, 3.5 s). In accordance with the absorption coefficients of hemoglobin at 538 and 569 nm, light absorption changes at 538 nm were slightly larger than those at 569 nm. The biphasic time course of the signal at 620 nm suggests that Hbr concentration initially increased due to oxygen consumption of activated neurons, which was followed by a decrease in Hbr concentration below the baseline due to blood inflow outstripping oxygen consumption. On the other hand, the absorption increase at 569 nm can be explained by the increase in Hbt resulting from the increase in blood inflow.

Spatial Patterns of Stimulus-specific Component of Intrinsic Signals

Unlike the stimulus-nonspecific components of the intrinsic signals, the polarity of the stimulus-specific components did not change at these wavelengths (Fig. 3*B*). Thus, to visualize the spatial patterns of the stimulus-specific components, we first temporally averaged the intrinsic signals from 1 to 7 s after stimulus onset. Then, the differential images of the signals were calculated by subtracting the temporally averaged images for one orientation from those for the orthogonal orientation (Fig. 4*A*). Even if the physiological sources of the signals seem to be different among these wavelengths, the spatial patterns of the stimulus-specific components were almost identical. The correlation coefficients between the differential images obtained at 620 nm and those at other wavelengths calculated on a pixel-by-pixel basis were significantly high (0.86 and 0.90 for the images obtained at 538 and 569 nm respectively; $P < 0.01$). We obtained consistent results for the other 13 cats: the average correlation coefficients for the 14 cats were 0.78 ± 0.08 for the images at 538 nm and 0.71 ± 0.09 for the images at 569 nm. These values indicate that there is a statistically significant correlation between differential images obtained at 620 nm and those obtained at other wavelengths ($P < 0.01$). These results indicate that the intrinsic signals recorded at these three wavelengths have a sufficient spatial resolution to resolve orientation-specific columnar organizations.

To estimate their spatial resolution quantitatively, we calculated the distance between neighboring iso-orientation domains and the size of the domains from the autocorrelation maps of differential images (see Materials and Methods). Figure 4*B* shows an example of the autocorrelation map of a differential image at 569 nm and its spatial profiles along the broken line that connects the central and adjacent peaks. In this example, the distance between neighboring iso-orientation domains was estimated to be 1.38 mm from the profile, and the full width at half-maximum (FWHM) of the profile's central peak was 0.65 mm. The average spatial separation between iso-orientation domains for the 14 cats was 1.34 ± 0.29 mm, and the average FWHM was 0.58 ± 0.12 mm (mean ± SD). Accordingly,

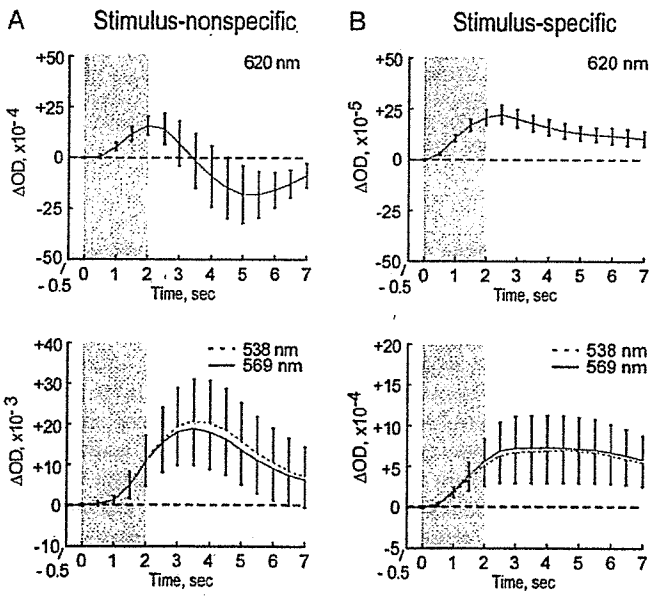

Figure 3. Time courses of stimulus-nonspecific and stimulus-specific components of intrinsic signals. (*A*) Time courses of intrinsic signals for stimulus-nonspecific components. Upper panel: 620 nm, Lower panel: 538 nm (dotted line) and 569 nm (solid line). (*B*) Time courses of intrinsic signals for stimulus-specific components. Upper panel: 620 nm, Lower panel: 538 nm (dotted line) and 569 nm (solid line). Error bars indicate one standard deviation (SD) of mean obtained from 14 cats. The shaded region indicates the duration of stimulus presentation. The horizontal broken line indicates the baseline corresponding to no absorption change.

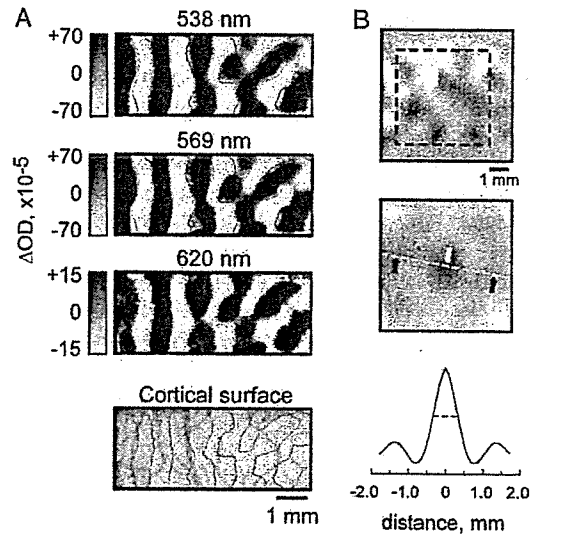

Figure 4. Spatial patterns of stimulus-specific components of intrinsic signals. (*A*) Differential images obtained from intrinsic signals at three wavelengths. The images were obtained by subtracting the responses to a grating at 90° orientation from those to a grating at 0° orientation. Black and white patches are specific to gratings at 0° and 90° orientations, respectively. Borders between active and less-active domains at 620 nm (red lines) are superimposed on each panel. This result and the result in Figure 2 were obtained from the same cortical ROI. (*B*) The analysis of spatial separations of neighboring iso-orientation domains and the domain sizes. Top panel: a differential image at 569 nm, where black and white patches are specific to gratings at 0° and 90° orientations, respectively. The grayscale range of ΔOD is $\pm 3.7 \times 10^{-4}$. The dotted rectangle (3.5×3.5 mm^2) in the differential image indicates the ROI for the analysis. Middle panel: the autocorrelation map of the ROI. White and black arrows indicate the largest peak (central peak) and secondary largest peaks on the map, respectively. Bottom panel: the spatial profile of the autocorrelation map along the broken line in the middle panel. The horizontal broken line in this profile indicates the FWHM of the central peak.

the spatial resolution of intrinsic signals at 569 nm was as high as 0.58 mm.

Measurement of Blood Volume Changes Based on Dye-specific Absorption Changes

Since intrinsic signals at 569 nm are considered to be proportional to Hbt concentration, the above analysis indicates that the blood volume component, as well as the Hbr component, has sufficient spatial precision to visualize individual iso-orientation domains in areas 17 and 18 of the cat visual cortex.

To further confirm our interpretation, we injected an absorption dye into the bloodstream and measured changes in blood volume on the basis of dye-specific absorption changes. Three observations provided evidence that the dye-specific absorption changes reflected changes in blood volume. First, the injections of the dye into the bloodstream caused a 17 ± 3% (mean ± SD, $n = 5$ cats) increase in light absorption. Second, the dye injections also increased the amplitude of the stimulus-nonspecific component of changes in absorption (Fig. 5*A*). The ratio of peak amplitudes before and after injections was 2.1 ± 1.1 (mean ± SD, $n = 5$). Thirdly, we found that the time courses of the stimulus-nonspecific component for the intrinsic signal at 569 nm were the same as those for the dye-specific absorption changes (Fig. 5*B*).

To examine whether stimulus-specific changes in blood volume are confined to iso-orientation domains, we compared differential images obtained before and after the dye injection (Fig. 6). If there were no stimulus-specific changes in blood volume, there would be no change in the differential image. However, the contrast of black and white patches in the differential image was in fact enhanced by the injection (Fig. 6*A*). For example, the magnitudes of stimulus-specific modulations became larger after the dye injection (Fig. 6*B*). We obtained similar results from all five cats. To quantify the results, we calculated the spatial and temporal averages (from 1 to 7 s after stimulus onset) of the stimulus-specific component of the intrinsic signals before and after the injections, and the magnitudes of the stimulus-specific components after the injections (vertical axis) were plotted against those before the injections (horizontal axis). As shown in Figure 6*C*, the magnitudes of the stimulus-specific components increased after dye injection in all five cats. These results support the proposal that there are stimulus-specific changes in blood volume.

Contribution of Changes in Blood Volume to the Intrinsic Signals in Awake Cats

To examine the blood volume component of intrinsic signals also in awake cats, we compared the intrinsic signals at 569 nm in anesthetized and awake states from the same cat. To avoid the effect of eye movements following the grating stimulus motion on the intrinsic signal in the awake state, we recorded the signal evoked by a flickering grating stimulus instead of a moving grating stimulus both in anesthetized and awake states in this experiment. We confirmed beforehand that these two stimuli elicited nearly the same responses in temporal patterns and identical response in the spatial patterns of iso-orientation domains in anesthetized cats (data not shown).

The time courses of intrinsic signals at 569 nm in the awake state were similar to those in the anesthetized state. The time to

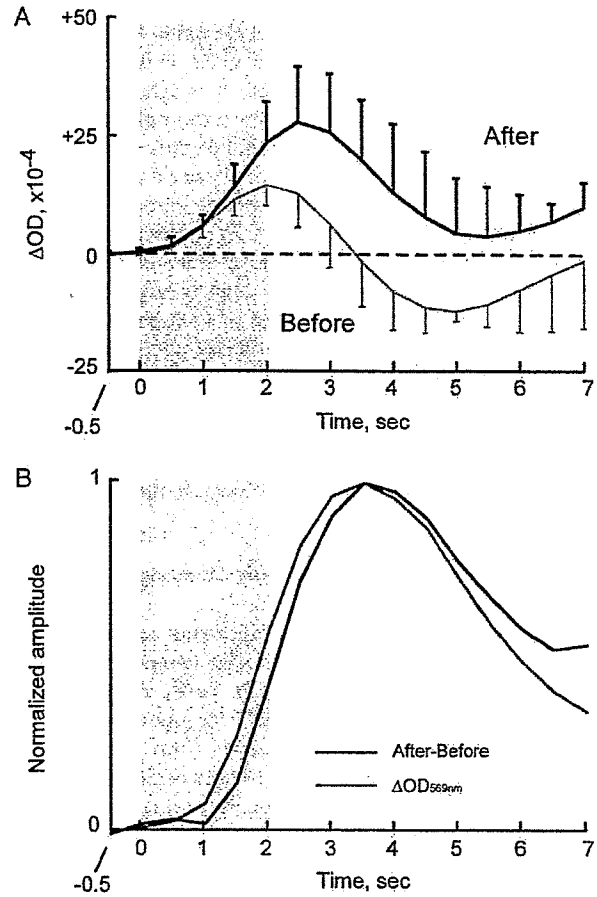

Figure 5. Contribution of blood volume changes to intrinsic signals. (*A*) Time courses of stimulus-nonspecific components of intrinsic signals at 620 nm before (orange line) and after (black line) dye injection. Error bars indicate one SD of mean obtained from five cats. (*B*) Comparison between the time course of intrinsic signals at 569 nm (green line) and that of dye-specific absorption changes (black line). Dye-specific absorption change was obtained by subtracting the absorption change at 620 nm before the injection (orange line in *A*) from that after the injection (black line in *A*). Each signal was normalized to their maximum values for comparison. The intrinsic signal at 569 nm shown here is the same data as in those shown in Figure 3*A*.

reach the peak (mean ± SD, $n = 5$ cats) of the intrinsic signal at 569 nm was 4.2 ± 0.6 s in the anesthetized state and 4.1 ± 0.46 s in the awake state. The spatial patterns of iso-orientation domains revealed by differential images at 569 nm in both states were almost identical (Fig. 7). Quantitatively, the correlation coefficient between the two images was 0.77 in this example. This value and the correlation coefficients obtained from the other four cats indicate that there is a statistically significant correlation between these images [average correlation coefficient: 0.74 ± 0.11 (mean ± SD); $P < 0.01$]. The average distance between neighboring iso-orientation domains and the average FWHM for the five awake cats was 1.26 ± 0.31 and 0.60 ± 0.10 mm respectively (mean ± SD). These values are similar to those obtained from the above-mentioned anesthetized cats. These results suggest that stimulus-specific changes in blood volume are not specific to the anesthetized state.

A difference in the intrinsic signal between the anesthetized and awake states was the magnitude of the stimulus-nonspecific and -specific components (Fig. 8). Figure 8*A* shows the average signal magnitude when the intrinsic signal at 569 nm reached its

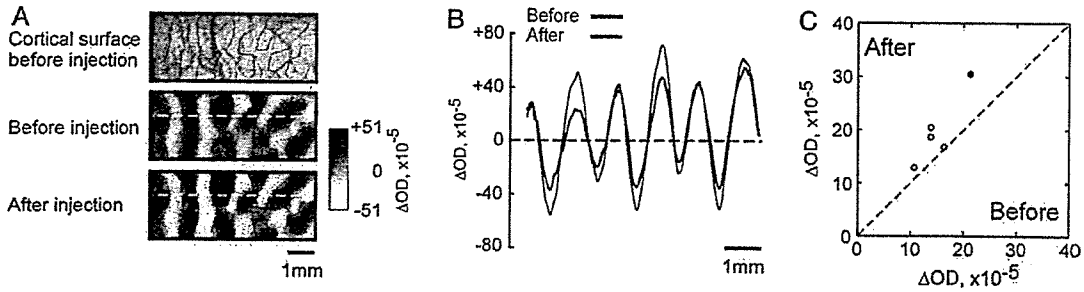

Figure 6. Stimulus-specific blood volume changes revealed by dye-specific absorption changes. (*A*) Spatial patterns of iso-orientation domains revealed by differential images before and after dye injection. The images were obtained by subtracting the responses to a grating at 90° orientation from those to a grating at 0° orientation and were temporally averaged from 1 to 7 s after stimulus onset. Borders between active and less-active domains before the injection (red lines) are superimposed on each panel. (*B*) Changes in signal intensities along the broken lines in the differential images of *A*. Black and red lines are the spatial profiles of stimulus-specific components before and after the dye injection, respectively. This result and the result shown in Figures 2 and 4*A* were obtained from the same cortical ROI. (*C*) The average magnitude of stimulus-specific components before (*x*-axis) and after (*y*-axis) the injection are plotted for five cats. Filled circle represents the result for the cat used in obtaining data shown in *A* and *B*.

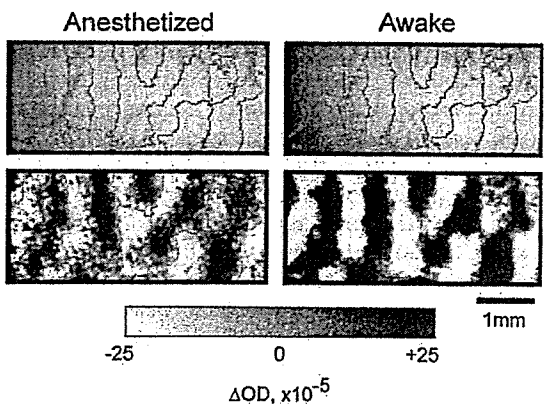

Figure 7. Maps of iso-orientation domains obtained from a cat in anesthetized and awake states. Upper panels: images of cortical surfaces taken at 538 nm from the same recording area in anesthetized and awake states. Lower panels: maps of iso-orientation domains revealed by differential images of intrinsic signals at 569 nm. The differential images were obtained by subtracting the responses evoked by an 8 Hz flickering grating at 90° orientation from the responses to a grating at 0° orientation and were temporally averaged from 1 to 7 s after stimulus onset. Borders between active and less-active domains at 569 nm in awake state (green lines) are superimposed on each panel. Recording from the anesthetized cat was conducted two days after that from the awake cats.

maximum (n = 5 cats). In the anesthetized state, neural activation induced increases in light absorption both in active and less-active domains corresponding to the stimulus-nonspecific component of the signals (Fig. 8*A*). The average magnitude of the stimulus-nonspecific component for the five cats was 15.7 × 10^{-3} in ΔOD. The increases in light absorption were always, though slightly, larger in the active domains of individual cats as shown by the difference in intrinsic signals between active and less-active domains (Fig. 8*B*). This difference corresponds to the stimulus-specific component of the intrinsic signal. The average magnitude of the stimulus-specific components for the five cats was 3.6 × 10^{-4} in ΔOD. Thus, the stimulus-specific component was only 2.3% of the stimulus-nonspecific component. The stimulus-nonspecific and stimulus-specific components of the intrinsic signal in the awake state were larger than those in the anesthetized state: the average magnitude of the stimulus-nonspecific components was 2.7 times larger and the average magnitude of stimulus-specific components was 3.6 times larger (Fig. 8*C*). The difference in magnitude ratio (2.7 versus 3.6) between stimulus-nonspecific and stimulus-specific components suggests that these two components have a different sensitivity to anesthesia.

Discussion

Spatial Localization of Changes in Blood Volume Elicited by Neural Activation

Several studies revealed the submillimeter-scale spatial localization of Hbr concentration changes in visual cortex (Malonek and Grinvald, 1996; Kim *et al.*, 2000; see also Thompson *et al.*, 2003). In this study, we examined the spatial precision of changes in blood volume using two different methods of analyzing reflection changes elicited by neural activation: (i) intrinsic signal imaging at the wavelength of the isosbestic point of hemoglobin, and (ii) analysis of stimulus-induced absorption changes of an intravenously infused dye. These analyses provide concrete evidence supporting a previous proposal that changes in blood volume are spatially localized (Frostig *et al.*, 1990). We showed that blood volume, as well as Hbr concentration, is precisely controlled at a submillimeter-scale resolution in areas 17 and 18 of the cat visual cortex in anesthetized and awake states.

It should be pointed out that a blood volume increase includes an intravascular space increase accompanied by the dilation of vessels (increase in plasma volume) and an increase in the number of red blood cells. The measurement of the intrinsic signal at 569 nm is sensitive to the increase in the number of red blood cells. On the other hand, it is considered that the increase in dye-specific absorption change reflects the increase in plasma volume. However, we cannot exclude the possibility that the dye-specific responses also reflect the increased number of red blood cells, since we did not quantitatively examine the possibility that the dye molecules were accumulated in or bound to red blood cells. Taking into account a previous *in vivo* microscopy study (Villringer *et al.*, 1994) demonstrating that increase of red blood cells in a capillary is associated with capillary dilation (i.e. increase of plasma volume) during hypercapnia, it is more plausible that these two effects — the increase in intravascular space and the increase in the number of red blood cells — are coupled and show similar behavior even when these changes are elicited by neural activation.

From the measurement of spatial separation and the size of the iso-orientation domains, we estimated the spatial resolution of blood volume changes to be as high as 0.6 mm. Recently,

Duong *et al.* (2001) have reported, using a CBF-based fMRI technique, that the size of iso-orientation domains was 0.47 mm. These results suggest that localization of blood flow changes is stronger than that of blood volume changes. In fact, unlike blood volume changes, Duong *et al.*'s experiment did not show any apparent stimulus-nonspecific component of CBF changes. They reported that the average CBF percentage-change ratio of the 'active' to 'inactive' domains was 3.3. This means that the stimulus-specific component of CBF changes was ~70% of the stimulus-nonspecific component. In contrast, this percentage was 2.3% in our measurement of blood volume changes. Further examinations are required to confirm these findings.

Limitation of Analyses of Intrinsic Signals at Multiple Wavelengths

Our analysis of intrinsic signals at multiple wavelengths is based on the assumption that intrinsic signals at visible wavelengths mainly reflect absorption changes of hemoglobin. According to this assumption, we used intrinsic signals at 569 nm as a measure of blood volume changes. We found that the time course of the intrinsic signals at 569 nm was similar to that of the dye-specific absorption changes, which supported the findings of this approach.

Although there was some supporting evidence for intrinsic signals at the isosbestic point of hemoglobin as a measure of blood volume, the isolation of components in intrinsic signals by the recording wavelengths may not be exclusive. For example, components other than hemoglobin absorption changes, such as Ls changes (MacVicar and Hochman, 1991; Kreisman *et al.*, 1995; Holthoff and Witte, 1996; Momose-Sato, 1998; Andrew *et al.*, 1999; Maheswari *et al.*, 2003; Sato *et al.*, 1997; see also Tomita *et al.*, 1983), may be involved in intrinsic signals. One way to better isolate individual components is to use a model that describes light reflection from the cortical surface (Malonek and Grinvald, 1996; Mayhew *et al.*, 1998; Nemoto *et al.*, 1999; Lindauer *et al.*, 2001). We have also analyzed our result using such a model and obtained results consistent with results described above (see Appendix). However, such analyses are not accurate and only provide semi-quantitative results because there is no exact model for changes in reflection from cortical surfaces.

Underlying Mechanisms of Stimulus-specific and Stimulus-nonspecific Components of the Blood Volume Component

In the present study, we have demonstrated that in the cat visual cortex the blood volume changes were resolved in individual iso-orientation domains ~0.6 mm in size. Taking into account the fact that the spatial separation of arteries is larger than that of functional domains, this finding suggests that fine mechanisms of blood volume control exist in fine vessel components, such as precapillary arterioles and capillaries whose spatial separations are definitely <0.6 mm (Pawlik *et al.*, 1981). The presence of such blood volume components is supported by anatomical studies showing contractile structures that may control blood flow and/or volume at the branching points of capillaries (Nakai *et al.*, 1981; Kuschinsky and Paulson, 1992; Shepro and Morel, 1993; Harrison *et al.*, 2002). This stimulus-specific component of blood volume changes, however, is only a small fraction of their stimulus-nonspecific component. To extract stimulus-specific changes in blood volume, for example, subtracting responses evoked by one orientation from those evoked by the orthogonal orientation is necessary in the visual cortex (see also for rodent barrel cortex, Hess *et al.*, 2000). There are three possibilities that explain the origins of stimulus-nonspecific components of the blood volume changes.

First, light scattering can limit the spatial resolution of optical measurement. Orbach and Cohen (1983) demonstrated that the light from a small 40 μm diameter spot spread to ~200 μm in diameter 500 μm away from the spot in cortical tissue. Because of this light scattering, stimulus-specific absorption changes can also spread into cortical domains related to the orthogonal stimulus. Thus, the stimulus-nonspecific component of the signals may be explained by the spread of the stimulus-specific component. If this is the case, however, it is difficult to explain the different ratios of signal magnitudes in the awake state to those in the anesthetized state between stimulus-specific and stimulus-nonspecific components (2.7 versus 3.6 in Fig. 8*C*).

Second, the distinction between stimulus-specific and stimulus-nonspecific components may be related to the specificity of neural activities coupled to the intrinsic signals. Assuming that synaptic activities are coupled to blood volume changes, blood volume changes can be elicited not only at regions where action potentials are generated but also at regions where

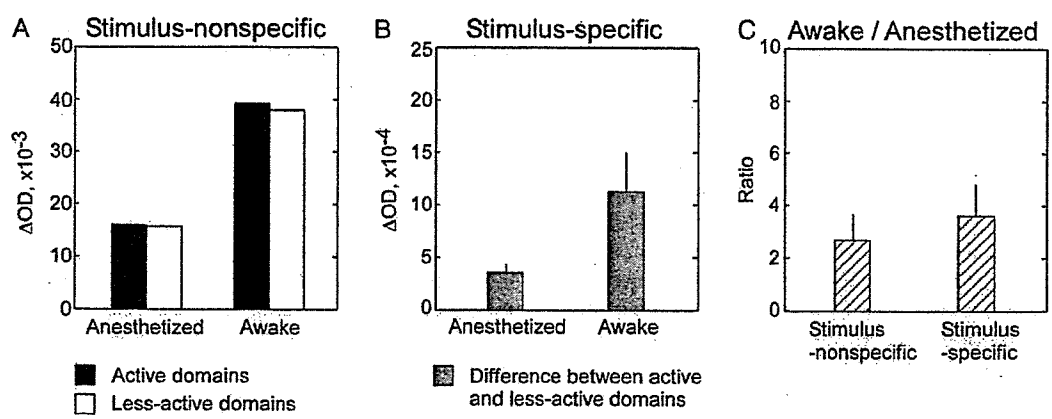

Figure 8. Comparison of signals related to blood volume changes between anesthetized and awake states. (*A*) Stimulus-nonspecific components of the intrinsic signal at 569 nm in active (solid bars) and less-active domains (open bars) for anesthetized (left column) and awake states (right column). The maximum amplitude of the signal in each cat was averaged and plotted ($n = 5$ cats). (*B*) Stimulus-specific components of the intrinsic signal at 569 nm in anesthetized (left column) and awake states (right column). (*C*) Ratios of the signal magnitude in the awake state to that in the anesthetized state for stimulus-nonspecific component (left column) and stimulus-specific component (right column). Error bars indicate one SD of mean obtained from five cats in *B* and *C*.

subthreshold synaptic potentials are generated. The stimulus-nonspecific component may reflect subthreshold synaptic potentials elicited regardless of the stimulus orientation. The mechanisms of coupling between neural activities and intrinsic signals remain issues for future investigations.

Finally, as the most plausible possibility, we consider the contribution of distinct mechanisms of blood flow control in small (precapillary, capillary) and large vessels (artery). Neural activations induce blood flow increases in arteries (Ngai *et al.*, 1988, 1995; Akgoren and Lauritzen, 1999). The arteries do not necessarily govern a particular iso-orientation domain. Blood flow increases in arteries should then induce nonspecific blood volume increases in downstream small vessels (precapillary, capillary and also probably arteriole), though these vessels have a submillimeter spatial precision (but see Iadecola *et al.*, 1997). Assuming supplemental blood flow control mechanisms in a capillary bed, we can expect stimulus-specific and -nonspecific components of blood volume changes. Because this proposal assumes two distinct control mechanisms, we can explain the different ratios of signal amplitudes in awake state to those in anesthetic state between stimulus-specific and stimulus-nonspecific components (Fig. 8*C*). Furthermore, the involvement of different vascular systems in the stimulus-specific and -nonspecific components of blood volume changes also explains the absence of correlation ($r = 0.43$, $P = 0.12$, $n = 14$) between the peak amplitudes of stimulus-specific and -nonspecific components.

Conclusions

In conclusion, we consider that blood volume signals in capillaries include both the stimulus-specific component controlled by the capillaries themselves and the stimulus-nonspecific component elicited by nonspecific blood inflow from upstream arteries. Because of these fine control mechanisms of blood volume, we were able to resolve submillimeter functional structures. The spatial resolution provided by these fine control mechanisms is at least 0.6 mm. This study also suggests that the visualization of blood volume changes can be used for studying brain functions at the submillimeter level.

Notes

We thank Justin Gardner for the development of a stimulus presentation program, and Kazushige Tsunoda for technical assistance throughout the experiments.

Address correspondence to Manabu Tanifuji, Laboratory for Integrative Neural Systems, RIKEN Brain Science Institute, 2-1 Hirosawa, Wako-shi, Saitama, 351-0198, Japan. Email: tanifuji@postman.riken.go.jp.

Appendix

The submillimeter-scale localization of blood volume change was also supported by an additional spectroscopic analysis as described below. We assumed that the change in optical density (ΔOD) was approximately expressed by a linear sum of changes in HbO_2 and Hbr concentrations (Δ[HbO_2] and Δ[Hbr] respectively), and Ls change (ΔLs) as follows:

$$\Delta OD(t)_\lambda = \varepsilon_\lambda^{HbO_2} \cdot d \cdot \Delta[HbO_2(t)] + \varepsilon_\lambda^{Hbr} \cdot d \cdot \Delta[Hbr(t)] - \Delta Ls(t) \qquad (2)$$

where ε_λ is the absorption coefficient at a wavelength, λ (see Fig. 1 legend for the values). The light path length, d, was assumed to be constant at these three wavelengths on the basis of our simulation study (data not shown; see also Shtoyerman *et al.*, 2000). Ls change is also

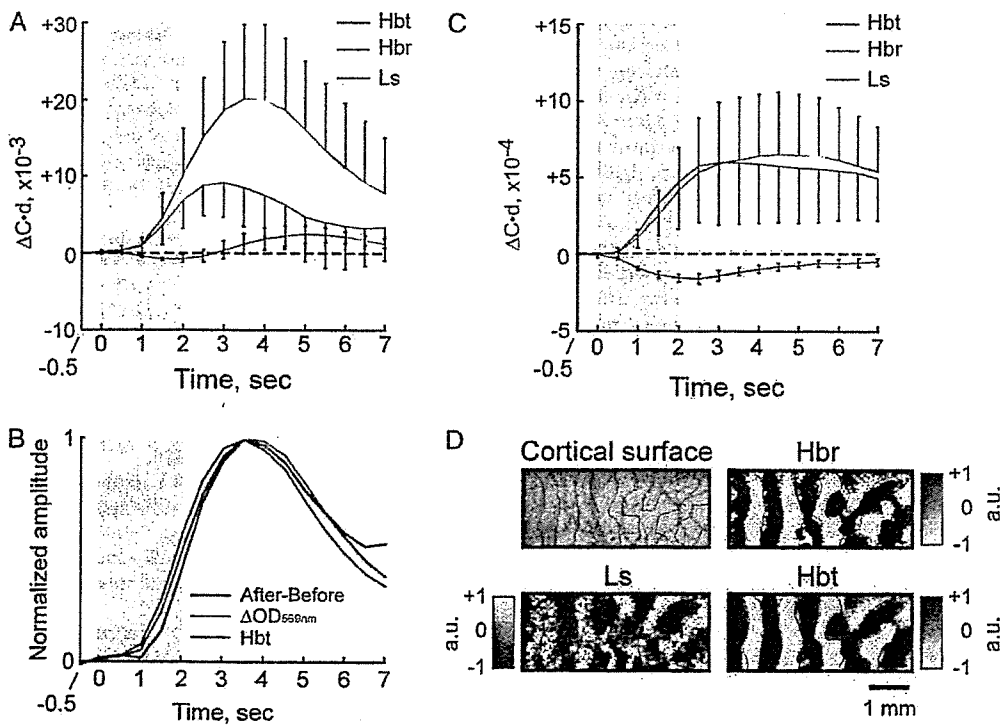

Figure 9. Results of spectroscopic analysis for intrinsic signals. (*A*) Time courses of stimulus-nonspecific components of Hbr, Hbt and Ls, which were calculated from the same data set shown in Figure 3*A*. Error bars indicate one SD of mean obtained from fourteen cats. (*B*) The time course of the Hbt (red line) was plotted together with the time courses of intrinsic signals at 569 nm (green line) and the dye-specific absorption changes (black line). Green and black lines are from the same data shown in Figure 5*B*. Each signal was normalized to its maximum values for comparison. (*C*) Time courses of stimulus-specific components of the Hbr, Hbt and Ls components. (*D*) Differential images obtained from the Hbr, Hbt and Ls. Borders between active and less-active domains at 620 nm (red lines) were superimposed on each panel. This result and the result shown in Figures 2, 4*A* and 6*A* were obtained from the same cortical ROI. Grayscales in Hbr, Hbt and Ls are arbitrary units.

assumed as a wavelength-independent variable on the basis of measurements of Ls changes in brain slices (unpublished observation; see also Cohen and Keynes, 1971; Salzberg *et al.*, 1985; Frostig *et al.*, 1990; Sato *et al.*, 1997; Momose-Sato *et al.*, 1998). The same equation was used in previous studies (Malonek and Grinvald, 1996) and yielded a good approximation for at least Hbr concentration changes in the cat visual cortex (Vanzetta and Grinvald, 1999; Thompson *et al.*, 2003).

To calculate the concentration changes of HbO_2, Hbr and the Ls component from intrinsic signals at 538, 569 and 620 nm, we analytically solved equation (2). The total hemoglobin (Hbt) concentration change was calculated as the sum of HbO_2 and Hbr concentration changes. The calculations were performed for individual stimuli and for control (blank screen) separately. Then, we subtracted the result calculated for the control (blank screen) from those for the stimuli. The product of the light path length, d, and the concentration of each component was used as a measure of each component, because d cannot be determined in the reflection measurement.

Figure 9*A* shows stimulus-induced changes in these three components. The time courses of the Ls component were biphasic, and did not vary greatly among the cats. The time courses of the Hbt concentration changes were monophasic and largely varied among the cats. To confirm whether the Hbt components faithfully represent blood volume changes, we compared the Hbt concentration changes with the stimulus-nonspecific components of the intrinsic signal at 569 nm (green line) and the dye-specific change (black line), and found these three signals showed very similar time courses (Fig. 9*B*). The time courses of the Hbr also varied among the cats. In 4 of 14 cats, the Hbr concentration initially increased after stimulus onset, reached a maximum and decreased below the baseline. However, in most cats, the changes in Hbr concentration did not cross the baseline. Consequently, the average time course of the Hbr concentrations for 14 cats was monophasic. The decrease in the Hbr concentration from the baseline in the late phase was not prominent in our study, but was in the previous studies (Malonek and Grinvald, 1996; Malonek *et al.*, 1997; Nemoto *et al.*, 1997, 1999; Mayhew *et al.*, 1999, 2000, 2001; Shtoyerman *et al.*, 2000, Jones *et al.*, 2001, Lindauer *et al.*, 2001). The discrepancy may be due to the following reasons. First, the solution based on the Beer-Lambert equation is largely affected by light pathlengths that may not be necessarily the same across the recording wavelengths used for the analysis (Mayhew *et al.*, 1999, Lindauer *et al.*, 2001). Second, time courses of intrinsic signals varied (e.g. at 607 nm, data not shown) since the relative contributions of Hbr, Hbt and Ls to the intrinsic signals may not be the same under different experimental conditions, such as individual specificity, anesthetic agents (Lindauer *et al.*, 1993), surgical procedure, recording area, stimulus type and species difference. For example, the time to reach the peak of the intrinsic signals depends on the stimulus frequency and duration (data not shown). Finally, there was no way to evaluate errors associated with the calculation of equation (2), since measurements from three wavelengths are used to obtain three parameters, the concentration changes of HbO_2, Hbr and the Ls component. Thus, in some of our measurements, we might fail to obtain reliable values of Hbr concentration changes, particularly late in the time course.

Similar to the intrinsic signals (Fig. 3*B*), the changes in Hbt and Hbr concentrations in active domains were always larger than those in less-active domains, and Ls changes in active domains were always smaller than those in less-active domains (Fig. 9*C*). To show the spatial pattern of the stimulus-specific components of Hbr, Hbt and Ls, their differential images were averaged from 1 s to 7 s after stimulus onset. As shown in Figure 9*D* the spatial pattern of the stimulus-specific component of the Hbt was almost identical to that of intrinsic signals (red contours) as well as the Hbr and Ls. The correlation coefficients between the differential images at 620 nm and that of Hbr, Hbt and Ls were 0.88, 0.87 and 0.77 ($P < 0.01$), respectively, in this example. We also calculated these correlation coefficients for the other 13 cats, and obtained statistically significant correlations for all of them ($P < 0.01$). The average correlation coefficients for 14 cats with Hbr, Hbt and Ls were 0.52 ± 0.17, 0.63 ± 0.17 and 0.79 ± 0.08, respectively. The highest correlation coefficient in the Ls is probably because of the relatively high contribution of the Ls to intrinsic signals at 620 nm.

References

Akgoren N, Lauritzen M (1999) Functional recruitment of red blood cells to rat brain microcirculation accompanying increased neuronal activity in cerebellar cortex. Neuroreport 10:3257–3263.

Andrew RD, Jarvis CR, Obeidat AS (1999) Potential sources of intrinsic optical signals imaged in live brain slices. Methods 18:185–196, 179.

Bonhoeffer T, Grinvald A (1991) Iso-orientation domains in cat visual cortex are arranged in pinwheel-like patterns. Nature 353: 429–431.

Bonhoeffer T, Grinvald A (1993) The layout of iso-orientation domains in area 18 of cat visual cortex: optical imaging reveals a pinwheel-like organization. J Neurosci 13:4157–4180.

Bonhoeffer T, Grinvald A (1996) Optical imaging based on intrinsic signals: the methodology. In: Brain mapping: the methods (Toga AW, Mazziotta JC, eds), pp. 55–97. San Diego, CA: Academic Press.

Bonhoeffer T, Kim DS, Malonek D, Shoham D, Grinvald A (1995) Optical imaging of the layout of functional domains in area 17 and across the area 17/18 border in cat visual cortex. Eur J Neurosci 7: 1973–1988.

Cannestra AF, Pouratian N, Shomer MH, Toga AW (1998) Refractory periods observed by intrinsic signal and fluorescent dye imaging. J Neurophysiol 80:1522–1532.

Cohen LB, Keynes RD (1971) Changes in light scattering associated with the action potential in crab nerves. J Physiol 212:259–275.

Duong TQ, Kim DS, Ugurbil K, Kim SG (2001) Localized cerebral blood flow response at submillimeter columnar resolution. Proc Natl Acad Sci USA 98:10904–10909.

Frostig RD, Lieke EE, Ts'o DY, Grinvald A (1990) Cortical functional architecture and local coupling between neuronal activity and the microcirculation revealed by *in vivo* high-resolution optical imaging of intrinsic signals. Proc Natl Acad Sci USA 87:6082–6086.

Ghose GM, Ts'o DY (1997) Form processing modules in primate area V4. J Neurophysiol 77:2191–2196.

Grinvald A, Lieke E, Frostig RD, Gilbert CD, Wiesel TN (1986) Functional architecture of cortex revealed by optical imaging of intrinsic signals. Nature 324:361–364.

Harrison RV, Harel N, Panesar J, Mount RJ (2002) Blood capillary distribution correlates with hemodynamic-based functional imaging in cerebral cortex. Cereb Cortex 12:225–233.

Hess A, Stiller D, Kaulisch T, Heil P, Scheich H (2000) New insights into the hemodynamic blood oxygenation level-dependent response through combination of functional magnetic resonance imaging and optical recording in gerbil barrel cortex. J Neurosci 20: 3328–3338.

Holthoff K, Witte OW (1996) Intrinsic optical signals in rat neocortical slices measured with near-infrared dark-field microscopy reveal changes in extracellular space. J Neurosci 16:2740–2749.

Iadecola C, Yang G, Ebner TJ, Chen G (1997) Local and propagated vascular responses evoked by focal synaptic activity in cerebellar cortex. J Neurophysiol 78:651–659.

Jones M, Berwick J, Johnston D, Mayhew J (2001) Concurrent optical imaging spectroscopy and laser-Doppler flowmetry: the relationship between blood flow, oxygenation, and volume in rodent barrel cortex. Neuroimage 13:1002–1015.

Kim DS, Duong TQ, Kim SG (2000) High-resolution mapping of iso-orientation columns by fMRI. Nat Neurosci 3:164–169.

Kreisman NR, LaManna JC, Liao SC, Yeh ER, Alcala JR (1995) Light transmittance as an index of cell volume in hippocampal slices: optical differences of interfaced and submerged positions. Brain Res 693:179–186.

Kuschinsky W, Paulson OB (1992) Capillary circulation in the brain. Cerebrovasc Brain Metab Rev 4:261–286.

Lindauer U, Villringer A, Dirnagl U (1993) Characterization of CBF response to somatosensory stimulation: model and influence of anesthetics. Am J Physiol 264:H1223–1228.

Lindauer U, Royl G, Leithner C, Kuhl M, Gold L, Gethmann J, Kohl-Bareis M, Villringer A, Dirnagl U (2001) No evidence for early decrease in blood oxygenation in rat whisker cortex in response to functional activation. Neuroimage 13:988–1001.

Maheswari RU, Takaoka H, Kadono H, Homma R, Tanifuji M (2003) Novel functional imaging technique from brain surface with optical

coherence tomography enabling visualization of depth resolved functional structure *in vivo*. J Neurosci Methods 124:83-92.
MacVicar BA, Hochman D (1991) Imaging of synaptically evoked intrinsic optical signals in hippocampal slices. J Neurosci 11:1458-1469.
Malonek D, Grinvald A (1996) Interactions between electrical activity and cortical microcirculation revealed by imaging spectroscopy: implications for functional brain mapping. Science 272:551-554.
Malonek D, Tootell RB, Grinvald A (1994) Optical imaging reveals the functional architecture of neurons processing shape and motion in owl monkey area MT. Proc R Soc Lond B Biol Sci 258:109-119.
Malonek D, Dirnagl U, Lindauer U, Yamada K, Kanno I, Grinvald A (1997) Vascular imprints of neuronal activity: relationships between the dynamics of cortical blood flow, oxygenation, and volume changes following sensory stimulation. Proc Natl Acad Sci USA 94:14826-14831.
Mayhew J, Hu D, Zheng Y, Askew S, Hou Y, Berwick J, Coffey PJ, Brown N (1998) An evaluation of linear model analysis techniques for processing images of microcirculation activity. Neuroimage 7:49-71.
Mayhew J, Zheng Y, Hou Y, Vuksanovic B, Berwick J, Askew S, Coffey P (1999) Spectroscopic analysis of changes in remitted illumination: the response to increased neural activity in brain. Neuroimage 10: 304-326.
Mayhew J, Johnston D, Berwick J, Jones M, Coffey P, Zheng Y (2000) Spectroscopic analysis of neural activity in brain: increased oxygen consumption following activation of barrel cortex. Neuroimage 12: 664-675.
Mayhew J, Johnston D, Martindale J, Jones M, Berwick J, Zheng Y (2001) Increased oxygen consumption following activation of brain: theoretical footnotes using spectroscopic data from barrel cortex. Neuroimage 13:975-987.
Momose-Sato Y, Sato K, Hirota A, Kamino K (1998) GABA-induced intrinsic light-scattering changes associated with voltage-sensitive dye signals in embryonic brain stem slices: coupling of depolarization and cell shrinkage. J Neurophysiol 79:2208-2217.
Nakai K, Imai H, Kamei I, Itakura T, Komari N, Kimura H, Nagai T, Maeda T (1981) Microangioarchitecture of rat parietal cortex with special reference to vascular 'sphincters'. Scanning electron microscopic and dark field microscopic study. Stroke 12:653-659.
Narayan SM, Esfahani P, Blood AJ, Sikkens L, Toga AW (1995) Functional increases in cerebral blood volume over somatosensory cortex. J Cereb Blood Flow Metab 15:754-765.
Nemoto M, Nomura Y, Tamura M, Sato C, Houkin K, Abe H (1997) Optical imaging and measuring of local hemoglobin concentration and oxygenation changes during somatosensory stimulation in rat cerebral cortex. Adv Exp Med Biol 428:521-531.
Nemoto M, Nomura Y, Sato C, Tamura M, Houkin K, Koyanagi I, Abe H (1999) Analysis of optical signals evoked by peripheral nerve stimulation in rat somatosensory cortex: dynamic changes in hemoglobin concentration and oxygenation. J Cereb Blood Flow Metab 19:246-259.
Ngai AC, Ko KR, Morii S, Winn HR (1988) Effect of sciatic nerve stimulation on pial arterioles in rats. Am J Physiol 254:H133-139.
Ngai AC, Meno JR, Winn HR (1995) Simultaneous measurements of pial arteriolar diameter and laser-Doppler flow during somatosensory stimulation. J Cereb Blood Flow Metab 15:124-127.
Orbach HS, Cohen LB (1983) Optical monitoring of activity from many areas of the *in vitro* and *in vivo* salamander olfactory bulb: a new method for studying functional organization in the vertebrate central nervous system. J Neurosci 3:2251-2262.
Pawlik G, Rackl A, Bing RJ (1981) Quantitative capillary topography and blood flow in the cerebral cortex of cats: an *in vivo* microscopic study. Brain Res 208:35-58.
Ratzlaff EH, Grinvald A (1991) A tandem-lens epifluorescence macroscope: hundred-fold brightness advantage for wide-field imaging. J Neurosci Methods 36:127-137.
Roe AW, Ts'o DY (1995) Visual topography in primate V2: multiple representation across functional stripes. J Neurosci 15:3689-3715.
Salzberg BM, Obaid AL, Gainer H (1985) Large and rapid changes in light scattering accompany secretion by nerve terminals in the mammalian neurohypophysis. J Gen Physiol 86:395-411.
Sato K, Momose-Sato Y, Arai Y, Hirota A, Kamino K (1997) Optical illustration of glutamate-induced cell swelling coupled with membrane depolarization in embryonic brain stem slices. Neuroreport 8:3559-3563.
Shepro D, Morel NM (1993) Pericyte physiology. FASEB J 7:1031-1038.
Shtoyerman E, Arieli A, Slovin H, Vanzetta I, Grinvald A (2000) Long-term optical imaging and spectroscopy reveal mechanisms underlying the intrinsic signal and stability of cortical maps in V1 of behaving monkeys. J Neurosci 20:8111-8121.
Sibson NR, Dhankhar A, Mason GF, Rothman DL, Behar KL, Shulman RG (1998) Stoichiometric coupling of brain glucose metabolism and glutamatergic neuronal activity. Proc Natl Acad Sci USA 95:316-321.
Silver IA (1978) Cellular microenvironment in relation to local blood flow. Ciba Found Symp:49-67.
Thompson JK, Peterson MR, Freeman RD (2003) Single-neuron activity and tissue oxygenation in the cerebral cortex. Science 299: 1070-1072.
Tomita M, Gotoh F, Yamamoto M, Tanahashi N, Kobari M (1983) Effects of hemolysis, hematocrit, RBC swelling, and flow rate on light scattering by blood in a 0.26 cm ID transparent tube. Biorheology 20:485-494.
Ts'o DY, Frostig RD, Lieke EE, Grinvald A (1990) Functional organization of primate visual cortex revealed by high resolution optical imaging. Science 249:417-420.
Tsunoda K, Yamane Y, Nishizaki M, Tanifuji M (2001) Complex objects are represented in macaque inferotemporal cortex by the combination of feature columns. Nat Neurosci 4:832-838.
Vanzetta I, Grinvald A (1999) Increased cortical oxidative metabolism due to sensory stimulation: implications for functional brain imaging. Science 286:1555-1558.
Villringer A, Them A, Lindauer U, Einhaupl K, Dirnagl U (1994) Capillary perfusion of the rat brain cortex. An *in vivo* confocal microscopy study. Circ Res 75:55-62.
Wang G, Tanaka K, Tanifuji M (1996) Optical imaging of functional organization in the monkey inferotemporal cortex. Science 272: 1665-1668.
Wang G, Tanifuji M, Tanaka K (1998) Functional architecture in monkey inferotemporal cortex revealed by *in vivo* optical imaging. Neurosci Res 32:33-46.

Chapter 12

Neural representation of object images in the macaque inferotemporal cortex

Manabu Tanifuji, Kazushige Tsunoda, and Yukako Yamane

12.1 Introduction

Information about visually presented objects is transmitted from the primary visual cortex (V1) to the inferotemporal cortex (IT) through multiple prestriate areas in macaque monkeys. To understand neural mechanisms of perception and recognition of objects through their visual images, response properties of neurons in the anterior part of the IT cortex, defined architectonically as area TE, have been investigated extensively. Because of the position- and size-invariant response properties of those neurons, this area is believed to correspond to lateral occipital cortex (LOC) in the human ventral visual pathway (Malach *et al.* 1995).

Physiological recording experiments have shown neurons responding equally well to object images and to visual features that are geometrically less complex than the object images (Desimone *et al.* 1984; Tanaka *et al.* 1991; Kobatake and Tanaka 1994). In particular, Tanaka and colleagues explored the simplest visual feature that maximally activates individual neurons in area TE ('critical feature'), using anesthetized monkeys. They found that critical features of many neurons in area TE are moderately complex. Figure 12.1 shows a representative critical feature extracted according to their method. These results indicate that an object is represented as combinations of visual features extracted by these neurons. However, these response properties of neurons in area TE have been investigated by extracellular recording of neuronal firing, and only a small number of neurons can be examined simultaneously. Thus, our understanding of object representation by these neurons in area TE is still at an early stage.

On the other hand, some other studies reported on neurons responding specifically to visual images that are familiar to the animals, such as faces or body parts (Gross *et al.* 1972; Perrett *et al.* 1982; Desimone *et al.* 1984; see also Fig. 12.11). Furthermore, several studies have investigated visual responses of neurons in monkeys trained with a particular set of visual stimuli, and revealed that some neurons specifically responded to

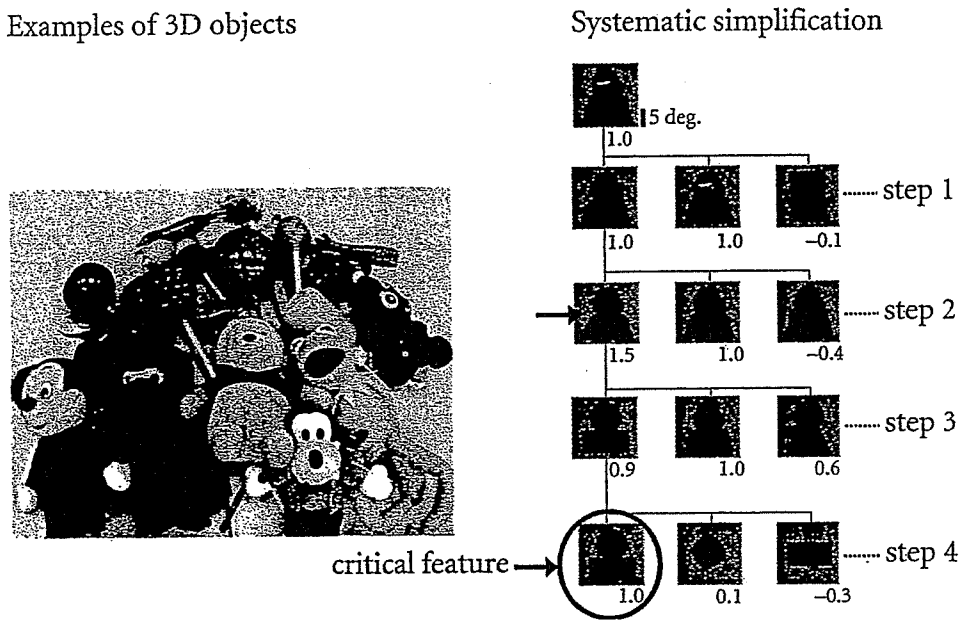

Fig. 12.1 The 'critical feature', the visual feature that maximally activates each cell, is determined by systematic stimulus simplification of the best object stimulus. First, we tested the cell with various three-dimensional objects, including faces, hands, stuffed animals, plastic fruits and vegetables, and paper mounts (left panel for some examples). After determining the best stimulus, we simplified it step by step to find the simplest stimulus that maximally activates the cell (right panel). For example, at step 1, we compared the best coloured object with its silhouette, and found that the silhouette activated the cell equally well. The rightmost rectangle was taken as a control stimulus. The numbers below each picture indicate the response amplitudes normalized to the response to the reference stimulus, the best object. The stimulus that evoked at least more than 70% of the response elicited by the best stimulus in the previous step, was again examined in the next step as the reference stimulus. At step 2, we examined the effect of the 'sharpness' of the corner at the junction of upper and lower parts (arrow), and found that the silhouette with the sharp corners was the most effective stimulus. From left to right, the stimuli were the silhouette with sharp corners, the silhouette that evoked the best response at the previous step, the silhouette without corners. Further simplification was carried out at step 3. Finally, we determined the critical feature as a combination of a circle and a rectangle because neither the upper nor lower part alone activated the cell.

visual stimuli that became familiar through training (Logothetis *et al.* 1995; Kobatake *et al.* 1998). The relationship between these neurons and those responding to visual features is also an issue that needs to be investigated.

Recently, intrinsic signal imaging has enabled us to reveal the spatial distribution of neurons activated by object images and to investigate response properties of neurons in characteristic sites revealed by intrinsic signal imaging. By this new approach, we have begun to understand more about object representation in area TE.

12.2 Intrinsic signal imaging

Neurons with similar response properties are clustered into a column in area TE (Gochin *et al.* 1991; Fujita *et al.* 1992). Thus, intrinsic signal imaging of columnar activation can be used to investigate spatial patterns of activation (Wang *et al.* 1996, 1998; Tsunoda *et al.* 2001). Intrinsic signal imaging measures the decrease in the degree of light reflection elicited by neural activation from the exposed cortical surface using a CCD camera (Fig. 12.2) (Grinvald *et al.* 1999). These reflection changes are due to metabolic changes elicited by neural activation, including deoxygenation of hemoglobin in capillaries (Grinvald *et al.* 1999).

Intrinsic signal imaging in area TE revealed multiple spots elicited by visual stimulation. The mean size of the 'active spots' (Fig. 12.2d) was 0.50 ± 0.13 mm along the longer axis and 0.35 ± 0.09 mm along the shorter axis ($n = 94$). These dimensions agreed well with the size previously reported for a column of cells with similar responsiveness in this area (Gochin *et al.* 1991; Fujita *et al.* 1992). Although these reflection changes are not a direct measure of neural activation, intrinsic signals coincide well with the activity of neurons examined by conventional extracellular recordings (Fig. 12.3) (Tsunoda *et al.* 2001).

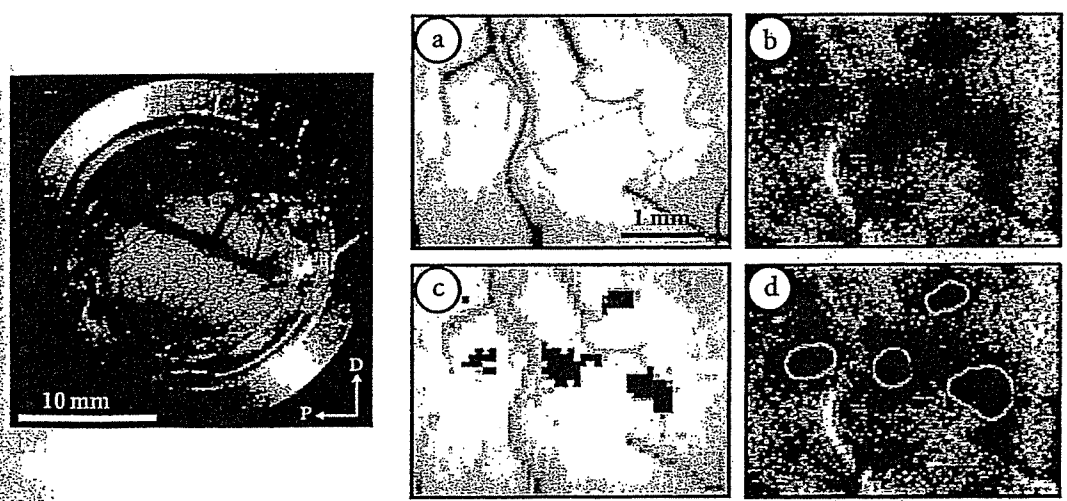

Fig. 12.2 Intrinsic signal imaging detects local modulation of light absorption changes in area TE. Surface view of the exposed portion of dorsal area TE (left panel). The thickest vessel running obliquely from the upper left to the lower right is along the superior temporal sulcus. The dorsal part of area TE is ventral to this vessel. (a) Portion of area TE where intrinsic signals were recorded. (b) A differential image showing a local increase in absorption. (c) Active regions, where the degree of reflection change evoked by the stimulus was significantly greater than that without the stimulus presentation. The region with the highest significance level is in red, that with the lowest significant level in yellow ($P < 0.05$). (d) Extracted active spots outlined by connecting pixels with 1/2 of the peak absorption value. (Modified from Tsunoda *et al.* 2001.)

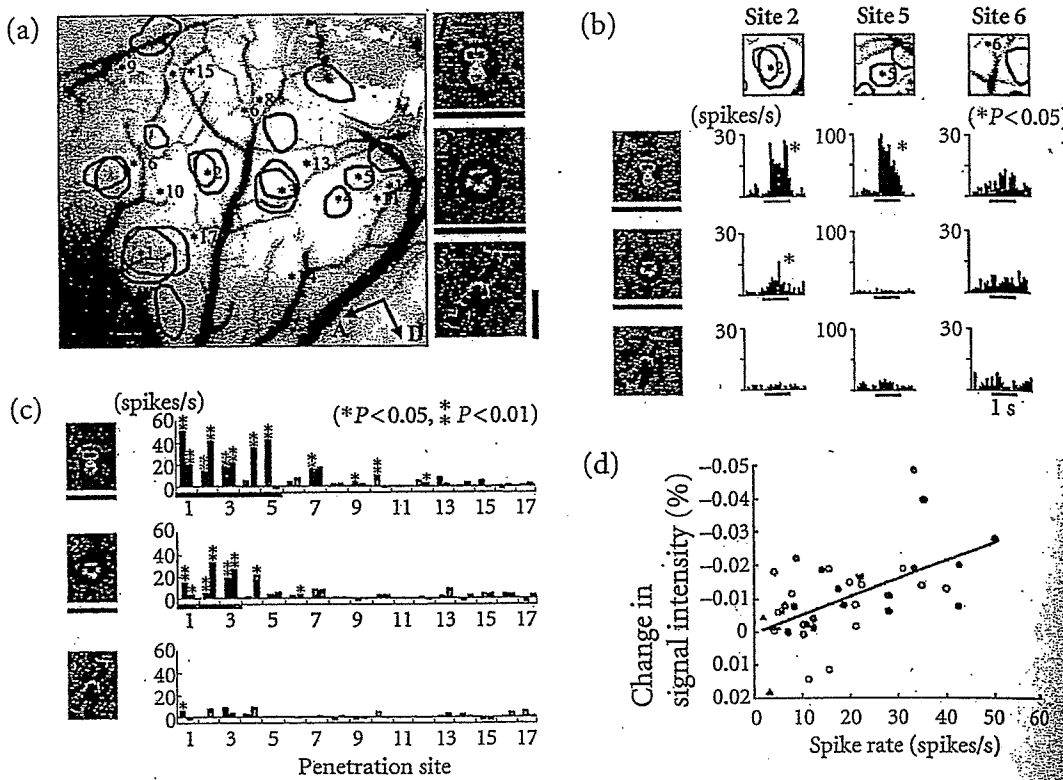

Fig. 12.3 Relationship between intrinsic signals and spike activity in area TE. (a) Active spots elicited by three different stimuli (*1*, *2* and *3*; on the right), and numbered electrode penetration sites. The color of individual contours indicates the active spots elicited by the stimulus underlined with the same color (same in all the figures showing spot distribution). A, anterior; D, dorsal. (b) Representative peristimulus–time histograms (PSTHs) showing the extracellular activity elicited by the three different stimuli, recorded at the sites indicated at the top of each column. Each row gives the PSTHs obtained following stimulation shown on the left side. Horizontal bars in the histograms indicate the one-second period for visual stimulation. (c) Mean firing rates evoked by the three different visual stimuli, for all 34 cells from 17 different sites. Two different cells separated by at least 200 μm were recorded at each penetration site. The penetration sites inside the active spots for a given stimulus were indicated by the colored bars in the top (red) and the second graphs (green). For stimulus 3, all the cells were recorded outside the active spot. (d) Correlation between the intensity of local changes of optical signal and evoked spike rates measured at the same cortical locations. Thirty-four cells were tested with 10 stimuli, and cellular activity with significant visual responses ($P < 0.05$) was plotted against the optical signal intensity obtained at the corresponding penetration sites for the individual stimuli. The activities of neurons from the same site were averaged. Different symbols indicate the responses at different sites. The regression line is given by $Y = -5.05e-6 + 5.46e-6X$ with a correlation coefficient of 0.57 ($n = 41$). Calibration bar, 10 degrees for the stimulus size in (a). Significance of difference determined by the Kolmogorov–Smirnov test for individual cell response is indicated by single ($P < 0.05$) or double ($P < 0.01$) asterisks in (b) and (c). (The same as in Fig. 12.5.) (Adapted from Tsunoda *et al.* 2001.)

To relate the optical response specificity to the neural activities, we recorded extracellular activity from 34 neurons in 17 sites located inside and outside the active spots (Fig. 12.3a). The representative peristimulus–time histograms (PSTHs) showed that the neuron in site 2, where both stimulus *1* and *2* elicited significant intrinsic signals, was activated by these two stimuli, but not by stimulus *3* (Fig. 12.3b, left-hand column). Similarly, only stimulus *1* significantly activated the cell in site 5 (Fig. 12.3b, middle column) and none of the stimuli activated cells in site 6 (Fig. 12.3b, right-hand column). In summary, among 34 neurons, 28 cells (82.4%) showed the same responsiveness to stimulus *1* as indicated by the optical responses: eight active cells inside the spot and twenty inactive cells outside (top row) (Fig. 12.3c). Similar results were obtained for 32 out of 34 cells (94.1%) for stimulus *2* (second row), and for 33 out of 34 cells (97.1%) for stimulus *3* (bottom row). A large variation of neuronal responses within the active spots (ex. Fig. 12.3c) did not alter the agreement between the intrinsic signals and extracellular responses. First, the optical response intensity and the firing rates of individual neurons showed a statistically significant positive correlation ($P < 0.001$) (Fig. 12.3d). Secondly, the average extracellular responses inside the spots (24.9 ± 17.2 and 16.8 ± 11.6 spikes/s for stimuli *1* and *2*, respectively) were significantly larger than those outside the spots (4.30 ± 4.95 and 3.32 ± 4.72 spikes/s for stimuli *1* and *2*, respectively) (Fig. 12.3c). These results indicate that the intrinsic signal coincides well with the firing activity of neurons examined by conventional extracellular recordings.

It should be mentioned that, in all the extracellular recordings, we recorded extracellular responses from superficial layers of cortex that are less than 1 mm in depth. Thus, strictly speaking, an 'active spot' revealed by intrinsic signal imaging may not necessarily correspond to a 'column', which usually means a cluster of neurons with similar response properties extending vertically from surface to the white matter. In the following sections, we use 'spots' for our results obtained by intrinsic signal imaging and 'columns' when we interpret our result in relation to previous studies.

12.3 Object representations revealed by intrinsic signal imaging

Intrinsic signal imaging revealed that different complex objects activated spots with different distribution patterns, together with some common active spots (Fig. 12.3a). Assuming that each spot represented a particular visual feature, the spots activated by one object may represent visual features specific to that object, and the spots activated by multiple objects may represent features common among these objects. We examined this idea by comparing distribution patterns of active spots with those produced by systematically simplified stimuli (Fig. 12.4) (Tsunoda *et al.* 2001). For example, in one case, a 'black cat' (a, *1*) was simplified to its 'head' (a, *2*), and then to the 'silhouette of its head' (a, *3*) (Fig. 12.4a). The original image (a, *1*) elicited 14 spots, but presenting the 'head' (a, *2*) elicited only eight of the original 14 spots. The silhouette (a, *3*) only activated three (yellow) of the eight spots elicited by the head (a, *2*). Similarly, Fig. 12.4b shows that spots A and B disappeared but spot D remained when the 'handle' and

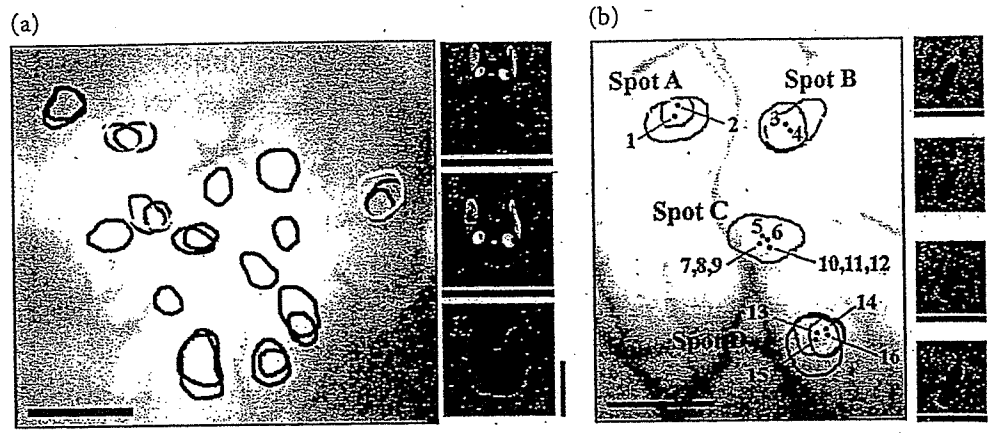

Fig. 12.4 Representation of complex object images and their simplification in area TE. (a) A case where simplified stimuli elicited only a subset of spots evoked by more complex stimuli. (b) Cases in which new spots appeared when the original stimulus was simplified. The numbers (1–16) indicate electrode penetration sites. (Modified from Tsunoda *et al.* 2001.)

'hose' were removed from the original stimulus, 'fire extinguisher'. In addition to the disappearance of spots, we found that new spots emerged by apparent simplification of an object: spot C appeared when the handle and hose were removed from the fire extinguisher. We have examined 12 pairs of activation patterns obtained before and after the simplification of the objects, and we observed changes in the distribution patterns consistent with either Fig. 12.4a or 12.4b for all of the pairs.

12.4 Visual features represented by individual spots

To directly address the neural mechanisms of appearance and disappearance of spots by object simplification, we recorded extracellular responses from 25 cells in the four spots shown in Fig. 12.4b, and analyzed the response properties of the cells in each spot. Figure 12.5 shows response properties of the representative cells in these spots. The difference in optical response patterns to stimuli *1* and *3* in Fig. 12.4b suggests that spots A and B represented visual features related to the handle and hose of the fire extinguisher. In fact, cells in spots A and B were significantly activated by the handle and hose in isolation (Fig. 12.5, a,*2* and b,*2*) as well as by the silhouette of the original fire extinguisher (Fig. 12.5, a,*1* and b,*1*). The cells in spot A were activated by the handle (Fig. 12.5, a,*3*) having protrusions, but not by the hose (Fig. 12.5, a,*4*). Furthermore, other stimuli with sharp protrusions, such as a 'hand' (Fig. 12.5, a,*5*) and cat's head (Fig. 12.5, a,*6*), also activated the cells. These cells seemed to require 'sharp protrusions' for activation. In contrast, cells in spot B were activated by the hose (Fig. 12.5, b,*4*), but neither by the handle (Fig. 12.5, b,*3*) nor a 'line segment' (Fig. 12.5, b,*5*). Thus, we determined the critical feature as an 'asymmetric arc' (Fig. 12.5, b,4). The neural responses of cells in spots C and D were consistent with the imaging results in Fig. 12.4b: cells in spot C were activated by the 'cylinder' but not by the original fire

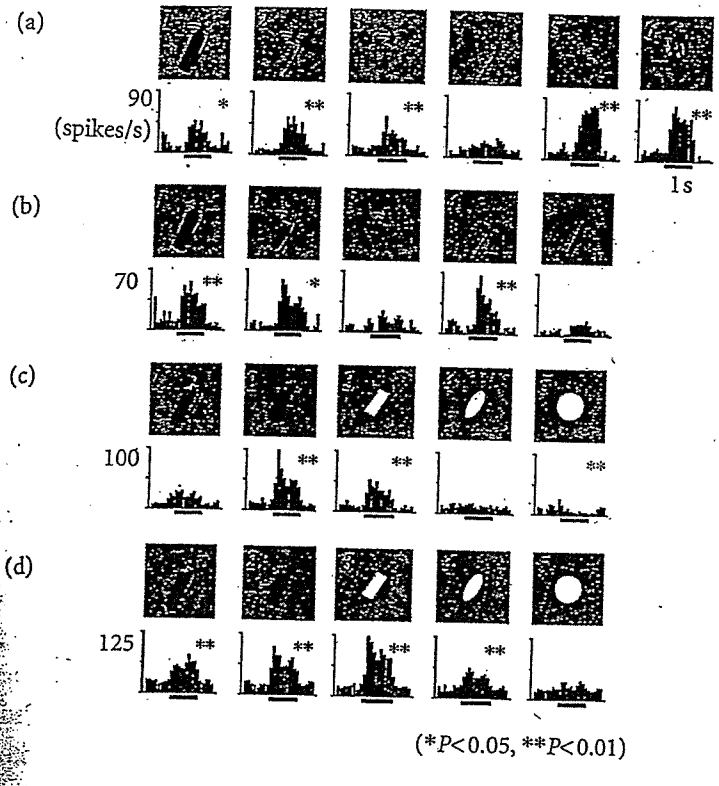

Fig. 12.5 Visual responsiveness of representative cells in spots A–D in Fig. 12.4b. (a), (b), (c), and (d) indicate responses in spots A (track 2, depth 620 μm), B (track 3, depth 540 μm), C (track 8, depth 280 μm), and D (track 16, depth 280 μm), respectively. Red asterisks indicate significant inhibition ($P < 0.01$). (Adapted from Tsunoda *et al.* 2001.)

extinguisher (Fig. 12.5, c,*1* and c,*2*), and cells in spot D were significantly activated by both stimuli (Fig. 12.5, d,*1* and d,*2*). The critical feature for cells in spot D was a 'rectangular shape' (Fig. 12.5, d,*3*), but cells also responded significantly to an 'ellipse' (Fig. 12.5, d,*4*). Since there was no response to a 'circle' (Fig. 12.5, d,*5*), we determined the critical feature of the spots as an 'elongated structure'.

Similarly, the simplest visual feature that could activate the cells in spot C was a rectangular shape (Fig. 12.5, c,*3*). In contrast to the cells in spot D, however, there was no activation by an ellipse (Fig. 12.5, c,*4*). In addition, the cells were inhibited by a circle (Fig. 12.5, c,*5*). Thus, these results suggest that the response properties of the cells in spot C (Fig. 12.4b) are determined by the balance between excitatory and inhibitory inputs: the excitatory inputs were given by a feature related to a rectangular shape and the inhibitory inputs are given by a feature related to a circle. This explanation would account for the lack of activation by the fire extinguisher, where the hose (circular shape) attached to the rectangular cylinder makes the entire shape elliptical. These results suggest that some of the columns representing a particular feature are inactive when other features are presented together with that feature. This could explain the optical imaging results in which active spots appeared following simplification of the stimulus.

The extracellular recording shows that inhibitory mechanisms are involved in the responsiveness of the neurons in spot C (Fig. 12.5, c,*5*). Fujita and Fujita (1996) found

intrinsic excitatory connections that extend parallel to the cortical surface for long distances. The underlying anatomical substrate of the inhibitory mechanisms could be combination of the excitatory connections and local inhibitory circuits within a target column. Alternatively, inhibitory neurons may extend their axons directly to distant target columns, as in the case of basket cells in the cat primary visual cortex (Kisvarday *et al.* 1994). One other possibility is that inhibitory interactions within area TEO is reflected in area TE through columnar projections from area TEO to area TE (Saleem *et al.* 1993).

12.5 Object representation with a combination of active and inactive columns

The combination of intrinsic signal imaging and extracellular recording can suggest the spatial layout of neural activity evoked by complex objects. Intrinsic signal imaging showed distributed representation of object images in area TE: object images are represented as combinations of multiple spots (Fig. 12.3a). In general, there are two concepts of distributed representation, depending on the fraction of neurons in the population: sparsely distributed and densely distributed representation (Foldiak and Young 1995). Although Fig. 12.3a shows many active spots elicited by some of the stimuli, the region activated by a single object image was, on average, only 3.3 ± 2.5% of the entire recording area (number of examined object images = 37). This low density suggests a sparsely distributed representation of objects. Another finding was that object simplification resulted in systematic changes in the distribution patterns of spots. We found that 32 out of 106 activity spots (30%) disappeared when part of the visual features were removed from the stimuli by object simplification (Fig. 12.4a). Extracellular recording showed that the optimal stimuli for neurons in these spots were visual features less complex than the original objects. These results suggest that there are spots specific for the representation of a particular visual feature within an object image, and that an object image is represented by a combination of spots specified for these visual features (Fig. 12.6a, b). However, among 106 activity spots, 18 spots appeared only after stimulus simplification (Fig. 12.4b, spot C). These results cannot be explained by this scheme, which implicitly assumes that all the spots related to a single feature in an object image are activated (Fig. 12.6b). Thus, we propose an extended scheme of distributed representation, where objects are represented not by the simple sum of feature columns but by combinations of active and inactive spots for individual features (Fig. 12.6c). According to this scheme, we think that the fire extinguisher in Fig. 12.4b was represented not only by the active spots representing the handle (spot A), the hose (spot B), and the cylinder (spot D), but by the absence of spot C representing the entire elliptical structure. Combinations of inactive as well as active columns increase the number of available activation patterns, and thus, in general, could increase the number of objects to be specifically represented (Fig. 12.6c). From a

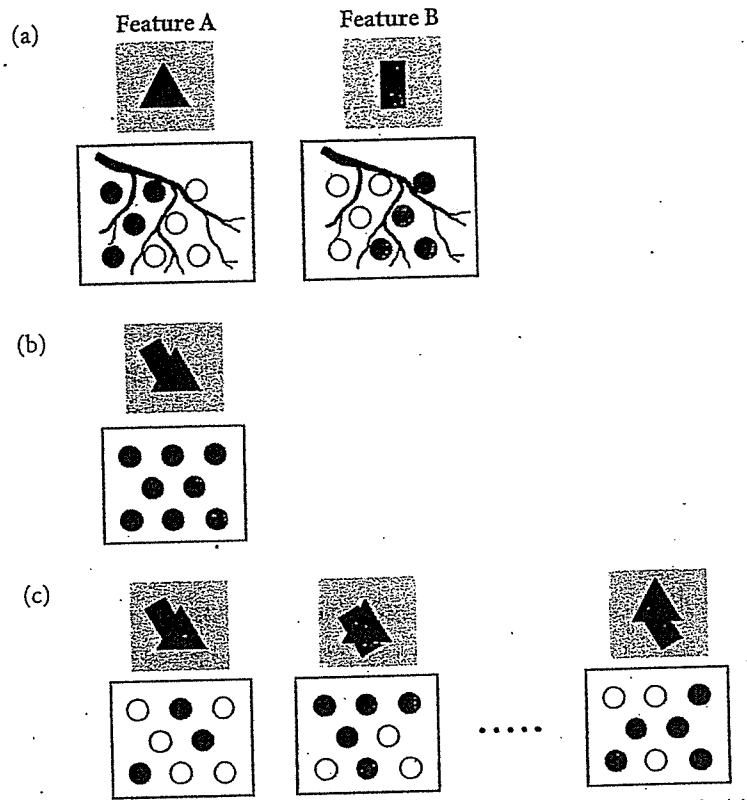

Fig. 12.6 Conventional and extended models of distributed representation of objects. Assuming that features A and B are represented by spots shown in red and blue, respectively, on the cortical surface (a), the visual stimulus consisting of these two features will activate all of these red and blue spots in models based on the conventional distributed representation (b). In our extended model, only a part of them are activated by the same stimulus (c). By this mechanism, stimuli consisting of the same features but arranged in different configurations can be represented by different activation patterns on the cortex. In each figure, the upper and lower panels indicate the visual stimulus and cortical area including spots responding to the stimulus.

physiological point of view, we consider the relationship between increased activation patterns and object representation in the following way:

In our scheme, we assume that a single visual feature maximally activates a set of columns (Fig. 12.6a). However, their tuning properties are not exactly the same, so that each column can represent additional information about visual images. For example, both spots C and D in Fig. 12.4b represent 'elongated structure'. But in addition, appearance of these spots depends on whether the given stimulus is elliptical or not. Then, objects differentiated by the additional information can be represented differently by activating a subset of these columns. One case would be representations of objects that consist of the same set of visual features but with a different arrangement of them. Another case would be representation of the same objects that look different under different vantage points, with partial occlusion, and with shading.

12.6 Representation of spatial arrangement of parts in object images

Examination of visual features represented by neurons in area TE suggested that at least some of the neurons in this area, represent 'local features' in object images, as neurons in spots A and B (Figs 12.4b and 12.5) represent 'protrusions' and 'asymmetric curvature', respectively. Since information about the spatial arrangement of 'local features' is necessary for the specific representation of object images, some of the other neurons may represent visual features related to the spatial arrangement of local features ('configurational information'). Here, we refer to 'local features' as visual features that occupy part of an object image and are distinguishable from other parts of an object image by their particular shapes, colors, or textures. 'Configurational information' is information about the spatial arrangement of "local features' themselves or about spatial arrangement of parts including local features. For example, intrinsic signal imaging with extracellular recording suggests that the presence or absence of activity in spot C constrains the spatial arrangement of the hose and the cylinder ('local features') of the fire extinguisher (Fig. 12.4b and Fig. 12.5c). This spot was activated when the hose is attached to the side of the cylinder and makes the entire shape elliptical, but may not be if the hose is secured above the handle where the rectangular shape of cylinder is exposed. Thus, we consider that activity in spot C has information about configuration to some extent, although this may be one way of representing a particular 'configurational information'.

To further examine the representation of 'configurational information', we investigated spots activated by an object (original, Fig. 12.7, 1) and the same object with a gap introduced between parts of the object (Fig. 12.7, 4), but not by a part alone (Fig. 12.7, 2 and 3) (Yamane *et al.* 2001). We suggest that these spots do not simply represent local features in objects, because either part is not essential for activation. Moreover, activation by the stimulus with an introduced gap indicates that local features appearing at

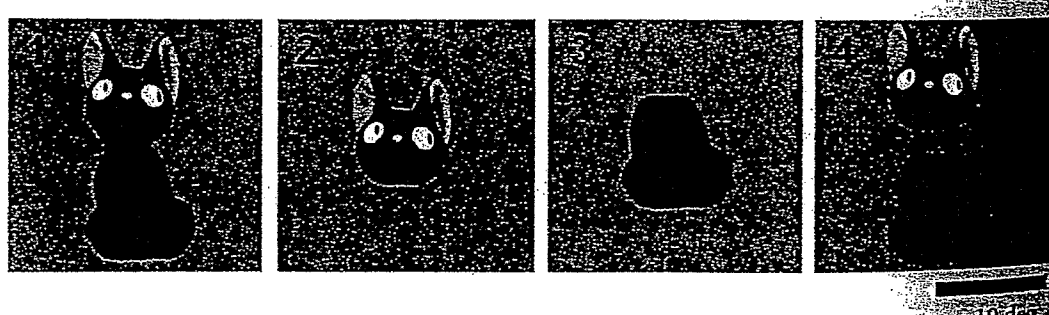

Fig. 12.7 A representative set of visual stimuli used in intrinsic signal imaging for examination of the representation of the spatial arrangement of parts. The response properties shown in Figs. 12.8 and 12.9 were obtained from a spot activated by stimuli 1 and 4, but not by stimuli 2 and 3.